In situ structural analysis with a SAXS laboratory beamline directly in a microfluidic chip

Radajewski Dimitri, Pierre Roblin, Patrice Bacchin, Martine Meireles, Yannick Hallez

▶ **To cite this version:**

Radajewski Dimitri, Pierre Roblin, Patrice Bacchin, Martine Meireles, Yannick Hallez. In situ structural analysis with a SAXS laboratory beamline directly in a microfluidic chip. Lab on a Chip, 2023, Lab Chip, 2023, 23, 3280, 23, pp.3280. 10.1039/D3LC00362K . hal-04245448

HAL Id: hal-04245448
https://hal.science/hal-04245448v1

Submitted on 17 Oct 2023

HAL is a multi-disciplinary open access archive for the deposit and dissemination of scientific research documents, whether they are published or not. The documents may come from teaching and research institutions in France or abroad, or from public or private research centers.

L'archive ouverte pluridisciplinaire **HAL**, est destinée au dépôt et à la diffusion de documents scientifiques de niveau recherche, publiés ou non, émanant des établissements d'enseignement et de recherche français ou étrangers, des laboratoires publics ou privés.

ARTICLE TYPE

Cite this: DOI: 00.0000/xxxxxxxxxx

In situ structural analysis with a SAXS laboratory beamline directly in a microfluidic chip.

Radajewski Dimitri,* Pierre Roblin, Patrice Bacchin, Martine Meireles, Yannick Hallez*

Received Date
Accepted Date

DOI: 00.0000/xxxxxxxxxx

Recent advances have been made in coupling microfluidic chips with X-ray equipment enabling structural analysis of samples directly in microfluidic devices.This important step mainly took place on powerful synchrotron facilities because of the need of a beam reduced in size to fit the microfluidic channel dimensions but still intense. In this work, we discuss how improvements of an X-ray laboratory beamline and an optimal design of a microfluidic device allow to obtain reliable structural information without the need of a synchrotron. We evaluate the potential of these new developments by probing several well known dispersions. These include dense inorganic gold and silica nanoparticles that scatter photons quite intensely, the bovine serum albumin (BSA) macromolecule, with more moderate contrast, to highlight possible applications in biology, and latex nanospheres with only weak contrast with the solvent to show the limits of the setup. We established a proof of concept for a versatile setup that will open the way for more complex lab-on-chip devices suitable for *in situ* and *operando* structural analysis by small angle X-ray scattering analysis without the necessity of a synchrotron source.

Introduction

Small-angle X-ray scattering (SAXS) has now been proven to be a powerful technique to investigate the structures and interactions of hard and soft matter systems.[1–3] It can provide a wide range of information and has been used extensively over the years to determine molecular interactions[4] and molecular weights,[5] , investigate structural conformations,[6,7] formation of nanoparticles[8–10] or folding dynamics of proteins in solution.[11,12]

Lab-on-chip devices have been developed more recently and offer the possibility to perform various operations at the microscale, using only small quantities of sample.[13,14] They are found in diverse scientific fields, such as biology, biochemistry, chemistry or physics. Among many examples, they can be used to mix fluids,[15,16] perform filtration[17–19] or compression[20] operations, observe crystallization phenomena,[21–23] separate blood cells[24,25] or carry out high-throughput screening.[26–28]

Coupling these two techniques has been recently successfully used to study nanoparticle formation,[29–34] protein folding and unfolding,[35–38] self-assembly of biomacromolecules[39,40] and lipid nanoparticles[41] or protein crystallization.[42,43] Microfluidic systems allow to perform unit operations with great control and reproducibility, with the possibility for segmented-flow configurations to quickly screen numerous experimental conditions and access to structural information in the compartmentalized units. Flowing samples ensures a constant renewal of the exposed sample and therefore avoids radiation damage.[44] Measuring at different positions in compartmentalized units allows *in situ* time-resolved analysis since the position in the channel and the timescale investigated are related by the flowrate. However, since the X-ray beam size has to fit the small size of the channel and at the same time suitable signal-to-noise ratio is needed, such experiments are commonly carried out at facilities equipped with high-brilliance synchrotron sources. Since access to them is limited, conducting long-term studies or performing experimental campaigns on demand is difficult.

At the same time, major technical developments concerning the performances of X-ray sources, detectors, X-ray optics and scatterless slits for *laboratory* X-ray beamlines[45,46] have opened the field for the use of microfocused beams at the laboratory scale. Microfluidic systems thus began to be used in conjunction with laboratory X-ray equipment to investigate the nucleation and growth of zinc oxide[47] and gold nanoparticles.[48,49] However, in these experiments, the microfluidic chip is basically used to synthesize the nanoparticles while the X-ray scattering is actually performed on a millimetric capillary glued at the exit of the chip. To our knowledge, there is a single report of a microfluidic device (made of PMMA, PTFE and Polyimide) directly mounted in a chamber of a laboratory X-ray instrument.[50] In this work, concentrated and dilute inorganic slurries (10 wt% silica nanoparticles vs. 0.5 wt% CaCO3 crystals) have been probed in segmented water-in-oil flows. The authors reported short time exposure SAXS images for concentrated silica nanoparticles contained in aqueous droplets

Laboratoire de Génie Chimique, Université de Toulouse, CNRS, INPT, UPS, Toulouse, France. E-mail: dimitri.radajewski@gmail.com, yannick.hallez@univ-tlse3.fr

flowing along a $300\times300\ \mu m^2$ channel. The quality of produced scattering pattern allowed a good agreement with a model for spherical particles. However for dilute calcite crystals almost zero scattering intensity was observed with small exposure times.

The advantages of using microfluidics are linked to the small lateral dimensions and depth of the channels. This imposes two major limitations when performing SAXS on a microfluidic chip: a small beam size to fit the lateral microfluidic channels dimensions, and a limited number of potential scatterers due to the small channel depth. This is not a problem when working with high brilliance synchrotron sources because the high flux will generate lots of scattered photons anyway, but it is a major issue limiting the joint use of laboratory beamlines with microfluidics. On laboratory beamlines, it is therefore very important to optimize X-ray optics (photon flux, beam size, smearing at small angles) together with microfluidic chip characteristics (channel geometry, materials, wall thickness) to minimize absorption and background scattering from the chip.

In this work, we report how a microfluidic device was developed and how a state-of-the-art laboratory beamline was optimized to perform *in situ*, *operando* SAXS measurements without the need for a synchrotron source. We evaluate the potential of these new developments by probing several well known types colloidal dispersions. These include dense inorganic gold and silica nanoparticles that scatter photons quite intensely, the bovine serum albumin (BSA) macromolecule, with more moderate contrast, to highlight possible applications in biology, and latex nanospheres with only weak contrast with the solvent to show the limits of the setup. This discussion is complementary to the one proposed in Ref. 50, in which additional constraints on the acquisition times allowed to have exploitable signals only for inorganic nanoparticles.

Material and methods

Microfluidic system

The microfluidic chip used in this work was fabricated using soft lithography and injection molding techniques.

First, the 2D design of the chip was produced with the Computer Aided Design software AutoCAD. It consists of four parallel, 400 μm wide, 3 cm long channels connected to inlet and outlet tubing (see Figure 1). The channel width was chosen to accommodate a relatively large beam size of about $250\,\mu$m, which allows to maximize the photon flux on the sample. Black circles are on the mask to form pillars that will favor a homogeneous distribution of OSTEMER during injection molding.

The next step is the fabrication of a master mold. Several layers of inexpensive multilevel negative tone photoresist dry film (WBR2000 series, DuPont, France) are first laminated on a glass substrate to obtain the required 400 μm thickness (Thermo Scientific Menzel-Glaser, Germany). The 2D chip design is then patterned on the dry film by UV exposure (UV-KUB2, Kloé, Montpellier, France) through a low cost emulsion mask, and 3D structures are obtained by developing the non-exposed photoresist using a 1%w solution of sodium carbonate (Na_2CO_3). After rinsing by tap water, the master is dried and hydrophobized with NOVEC^{TM} 1720 (3M, France).

A hollow PDMS (Sylgard 184 elastomer kit, Dow Corning, USA) mold is then produced by pouring liquid PDMS on the surface of the dry film master, curing it for few hours at 70°C before gently and easily peeling it off from the hydrophobic master mold. The procedure to elaborate the dry film master mold and the PDMS mold is described in more details in Ref. 42 for the interested reader.

To assemble the final microfluidic chip, two OSTEMER (Mercene Labs, Sweden[51]) stickers have to be prepared. First, a transparent mylar film is placed on top of the hollow PDMS mold and liquid OSTEMER is injected with a needle in the gap between the mold and the film (see Figure 1). OSTEMER is then UV-cured, becoming solid, but still flexible and sticky, so the structure can be peeled off from the PDMS mold. Second, another OSTEMER sticker is obtained by injecting and curing it in a flat $50\,\mu$m deep PDMS mold on top of which a $25\,\mu$m polyimide Kapton film is positioned. Finally, the two OSTEMER stickers are assembled together and a second curing of the whole chip is made by placing it in an oven at 90°C overnight. The mylar film used as a fabrication support can finally be removed to get the final chip made of only OSTEMER supported by a Kapton film.

PEEK capillaries $360\,\mu$m OD $150\,\mu$m ID (Trajan Scientific, United Kingdom) are used as connectors and epoxy-glued to the inlet and outlets of the chip. They are connected to PTFE tubing 1/16" OD with specific adaptors and colloidal dispersions are manually injected in the device with a syringe.

As this work is concerned by the optimization of a microfluidic chip for a use on a laboratory X-ray beamline with low photon flux compared to a synchrotron, the important point is that X-rays will pass through 25 μm of Kapton, two 50 μm thick layers of OSTEMER, and 400 μm of sample. Maximizing the sample thickness compared to the wall thickness is of course essential. Increasing the sample thickness further would be possible but the device would become closer to a standard capillary than to a microfluidic chip. Polyimide (Kapton) films and OSTEMER are known for their very good compatibility with SAXS measurements in particular due to their low attenuation and low background scattering.[31] The Kapton layer is present to provide some mechanical rigidity to the chip, and decreasing its thickness is not an option. Cutting a small window in this layer (or another support material) so the X-rays pass only through OSTEMER and the sample is however possible. Trying to reduce the OSTEMER thickness below 50 μm led to fluid leakage through microcracks, so the present thickness seems to be optimal to maximize the photon flux and minimize background scattering.

Small-Angle X-ray scattering

SAXS experiments were performed on a Xeuss 2.0 laboratory beamline from Xenocs equipped with a microfocus GeniX 3D Cu microsource and a Pilatus3 1M HPC detector from DECTRIS. Before modification, the X-ray beam was collimated with FOX3D 12_INF single reflection multilayer optics, and cut vertically and horizontally by two scatterless slits to minimize beam divergence. Two modifications of this setup have been performed to increase the photon flux while minimizing the beam size on the sample. First, the optics were replaced by a FOX3D HFVL mirror which allowed to increase the flux from 80 to 450 million photons per

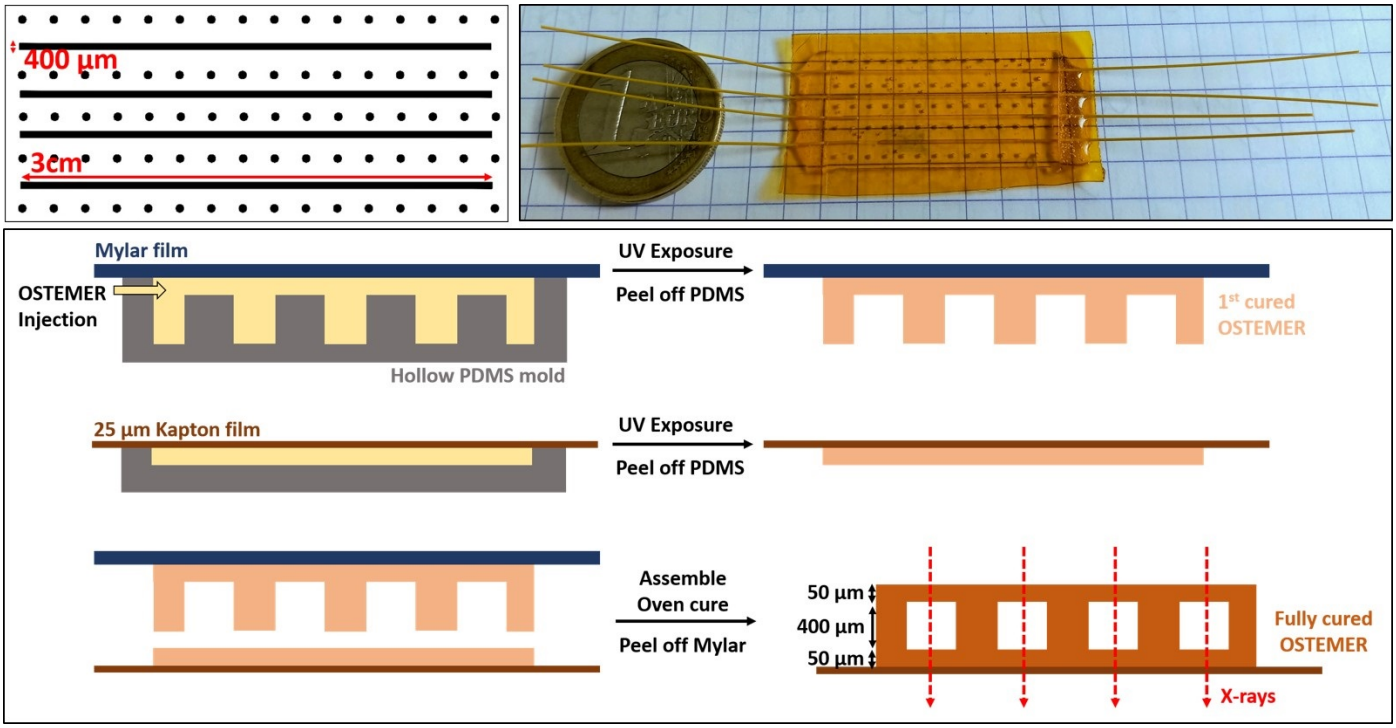

Fig. 1 Top left panel: design of the microfluidic chip consisting in four parallel $400\,\mu$m wide, 3 cm long channels. Top right panel: picture of the final chip with inlet/outlet capillaries. Bottom panel: fabrication process of an OSTEMER chip: first the two OSTEMER stickers are prepared by injection and curing in hollow PDMS molds, then they are assembled together and fully cured. For SAXS optimal acquisition, in this set-up, X-rays pass through $25\,\mu$m of Kapton, $50\,\mu$m of OSTEMER, $400\,\mu$m of sample and $50\,\mu$m of OSTEMER

second with fully open slits. Second, a square scatterless silicon nitride pinhole of cross-section 0.25×0.25 mm^2 from Silson was added after the last slit, at 2 cm from the sample (see Figure 2). The reason is twofold. With the original setup (12_INF mirror, no pinhole), obtaining a 0.25×0.25 mm^2 beam size on the sample was possible with relatively open slits. The flux was then about 1.5×10^6 ph s^{-1}. With the change to the more divergent HFVL optics, it became necessary to close the last slit located 32 cm upstream from the sample much more to preserve the beam size. As a result, the flux on the sample actually decreased to the very low value of 0.15×10^6 ph s^{-1}.

A similar issue was mentioned by Levenstein and coworkers[50] using the same Xeuss 2.0, with the same beam size, although their more powerful liquid-metal-jet source allowed them to maintain a flux of 3.7×10^6 ph s^{-1}. By inserting a pinhole located very close to the sample in our setup, the slits could be opened more than on the original setup and the flux on the sample could be increased back to about 9.5×10^6 ph s^{-1}. The flux on the sample is thus maximized and possible artifacts due beam divergence are minimized. With this setup, the divergence of the beam after the pinhole is about 1 mrad. The microfluidic chip is mounted on a support, fixed on a precise motorized translation stage such that it can be readily moved in horizontal and vertical positions with respect to the X-ray beam in order to position the investigated channel in front of the beam.

The sample to detector distance was 1.2195 m and the wavelength is $\lambda = 1.541$ Å giving a q-range extending from 0.005 Å^{-1} to 0.5 Å^{-1}. All measurements were performed at atmospheric pressure, 21 °C, and ambient humidity. For the relatively low scattering materials (proteins and latex), 6 acquisitions of 10 minutes were performed and the raw 2D scattered image was obtained by averaging the 6 recorded frames. For the most scattering materials (gold and silica nanoparticles), single acquisitions of 10 minutes were sufficient to have a decent scattering pattern. The recorded images were corrected for detector efficiency and distortion, scaled by the acquisition time, sample thickness, and sample transmission factor, and averaged in the azimuthal direction while applying a mask to remove faulty regions of the image to finally obtain the intensity profiles $I_s(q)$.

The intensity q of the scattering vector is

$$q = \frac{4\pi}{\lambda}\sin\frac{\theta}{2} \tag{1}$$

where θ is the scattering angle.

For each experiment, a background scattering profile $I_b(q)$ was also obtained from the buffer, using the same standardized scaling procedure. The final intensity profiles reported hereafter are defined as $I(q) = I_s(q) - I_b(q)$. For single scattering they can be written as

$$I(q) = A\phi P(q)S_m(q) \tag{2}$$

where A is a q-independent constant, ϕ is the colloid volume fraction, $P(q)$ is the form factor and $S_m(q)$ is the so-called measurable structure factor. At large dilution $S_m(q)\to 1$ so a measurement in these conditions gives $I_0(q) \equiv A\phi_0 P(q)$. A measurement at finite concentration then allows to define $S_m(q)$ and A from (2) and the requirement $S_m(q\to\infty) = 1$. Note that $S_m(q)$ is the

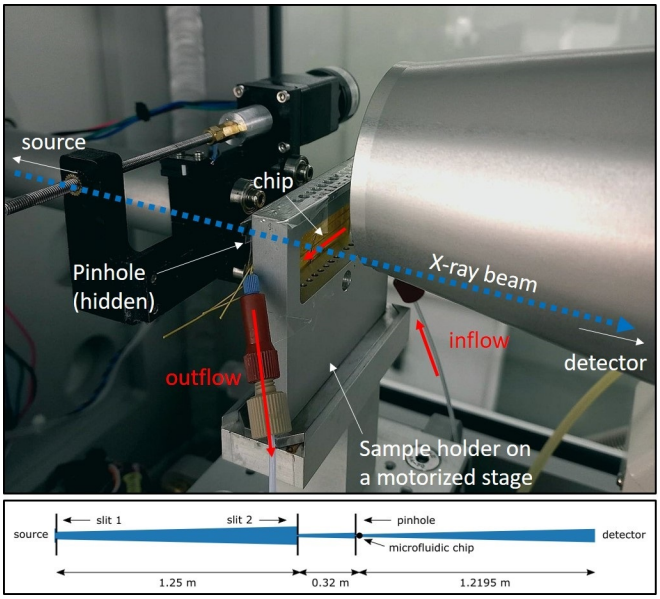

Fig. 2 Top: microfluidic chip on the Xeuss 2.0 SAXS beamline. The pinhole is located on the black motorized stage added to the standard setup. Bottom: schematic representation of the beamline showing the source emitting a wide beam (diameter about 1 mm), which is cut by slits 1 (0.7×0.7 mm^2) and 2 (0.3×0.3 mm^2), and by the pinhole (0.25×0.25 mm^2) located at 2 cm from the sample.

true structure factor only for monodisperse systems without correlations between positions and orientations. For polydisperse or anisotropic systems, $S_m(q)$ is merely an easily measurable quantity with no clear thermodynamic meaning.

Preparation of solutions

Gold nanoparticles were synthesized by collaborators (see Acknowledgements) using an adapted protocol from Ref. 52. A mixture of oleylamine and HAuCl4xH2O in pentane was stirred at room temperature for 5 min. Afterward, a solution of tert-butylamine borane in presence of oleylamine in pentane was added to reduce the gold precursor. The color of the solution immediately turned to brown. After stirring for 60 min at room temperature, the nanoparticles were purified by precipitating with ethanol and centrifuged. The supernatant was discarded and the precipitated NPs were redispersed in pentane at a volume fraction of 1.3×10^{-4}.

The aqueous dispersion of Ludox HS-40 (Sigma-Aldrich, France) colloidal silica 40 wt. % was filtered through a 5 μm teflon filter and then dialyzed for 15 days in a 7 kDa cellulose membrane bag (Sigma-Aldrich, France) against a 1mM potassium chloride solution. Subsequent dilutions of the washed dispersion were obtained with the 1mM KCl solution to reach volume fractions $\phi=$ 0.00234, 0.00496, 0.00826, 0.0144, 0.0287, 0.0420 and 0.0907. The volume fraction was determined by weighting a 2 g sample before and after drying at 120°C. For this calculation we assumed a silica density of 2200 kg m^{-3}.

Protein Bovine Serum Albumin (ThermoFisher Scientific, France) was used as a model macromolecule and was solubilized at a stock concentration of 100 mg/mL in phosphate-buffered saline PBS (Fisher BioReagents, USA). Subsequent dilutions led to 5, 12.5, 25 and 50 mg/mL solutions used in these experiments.

The aqueous dispersions of polystyrene latex beads with sulfate charges (Invitrogen, ThermoFisher Scientific, USA) were prepared using a 1 mM NaCl solution to reach volume fractions $\phi=$ 0.034, 0.07, 0.105, and 0.14. The average radius announced by the manufacturer was 13.5 nm.

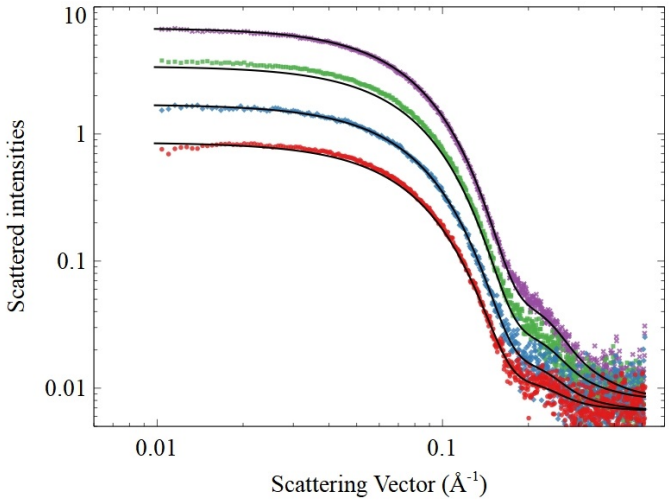

Fig. 3 Scattering data for gold nanoparticles and model for polydisperse spheres with radii following a Schulz distribution with average 2.75 nm and 17 % polydispersity. From top to bottom: dispersion as prepared, and diluted 2, 4, and 8 times.

Results and discussion

Gold nanoparticles

The first samples used to test the setup were dispersions of gold nanoparticles in pentane. These colloids are dense, spherical, and quite monodisperse so they are expected to have a very clear SAXS signature even at very low volume fraction.

Results are presented in Figure 3 together with model spectra corresponding to sphere suspensions in which particle radii follow a Schulz distribution[53] with average 2.75 nm and 17 % polydispersity. This is in good agreement with the specification from the synthesis protocol.[52]. The absolute intensity of the model (coefficient A in (2)) has been adjusted only once on the data corresponding to the highest concentration. The model spectra for the three other samples then follow eq. (2) without need for further adjustments.

As expected for these dense colloids, the signal to noise ratio is quite good, and sufficient to fit a form factor with confidence. It remains however too limited to use Porod's law[2,54] based on the high-q limit of Iq^4 quantitatively. For this, and for the present dispersion, the background noise would need to be negligible up to $q\simeq0.4$ Å^{-1}, which would require an increase of the scattered signal intensity by about two orders of magnitude. The Q invariant (integral of Iq^2) [2,54] could be calculated with reasonable accuracy in particular because the minimum q value has been made low enough with the use of the pinhole.

Silica nanoparticles and interactions

The test with gold nanospheres allowed to discuss pure form factor measurements. The next step is to test the possibility to mea-

sure the mesostructure of a dispersion, and therefore indirectly colloidal interactions, directly inside a microfluidic chip. For this purpose we used Ludox HS40 aqueous silica dispersions. These particles scatter X-rays quite intensely due to their large contrast, which makes SAXS measurements relatively easy. They have already been investigated using synchrotron sources (see e.g. Refs. 55–57) so their SAXS signature is quite well documented, and their surface chemistry is also well known. We are concerned here with the following questions: can the present setup yield spectra with good enough signal-to-noise ratios to fit the first structure factor peak? The second one? Can we access small enough angles to measure the plateau $S(q \to 0)$, which is important for thermodynamics?

The most dilute sample ($\phi = 0.00234$) was used to measure the form factor, which is reported in the inset of Figure 4. It could be modeled using a Schulz distribution for particle radii with an average of 8 nm and 13 % size polydispersity, in line with frequently reported values.[56–58] The measurable structure factors of the more concentrated samples are reported in Figure 4. The apparition of a marked structure peak and the decrease of $S(q \to 0)$ with increasing particle concentration could be observed clearly enough to compare them to theoretical model and simulation predictions. These features, due to long-range electrostatic interactions, could be computed theoretically by solving the Ornstein-Zernike (OZ) equation with the Rogers-Young closure and a Hard-Sphere-Yukawa effective potential (see Ref. 59 and references therein for more details). Polydispersity was accounted for using the decoupling approximation, shown to be quite accurate for the present moderate polydispersity.[53,60] The effective colloidal charge and screening length have been calculated using the Extrapolated Point Charge renormalization method,[61] accounting for a volume-fraction-dependent charge regulation mechanism involving the surface reaction

$$\mathrm{Si{-}OH} \rightleftharpoons \mathrm{Si{-}O^- + H^+} \qquad (3)$$

with a dissociation constant $pK = 7.5$, a surface concentration of ionizable sites $\Gamma^0 = 8\,nm^{-2}$, and a Stern capacitance $C_S = 2.9\,F.m^{-2}$. These values have been measured independently on large silica beads by Trefalt and coworkers.[62] The pH value of 6.9 used in the regulation model was the one directly measured in the dispersions. Considering there are several approximations in this theoretical model, and the fact that we did not use any fitting parameter, the agreement observed in Figure 4 is generally very good.

We also performed simulations of the two most concentrated systems using a special version of Brownian Dynamics that does not rely on the definition of effective pair potentials or on any decoupling approximation to handle polydispersity. In these simulations, the 3D electric potential field is computed throughout the suspension at every time step by solving the non-linear Poisson-Boltzmann equation. The excess osmotic stress tensor field is then calculated and integrated to obtain the many-body forces exerted on every colloid accurately.[63–66] The structure factors obtained from these simulations and from the theoretical model described above are in very good agreement (see open circles in Figure 4).

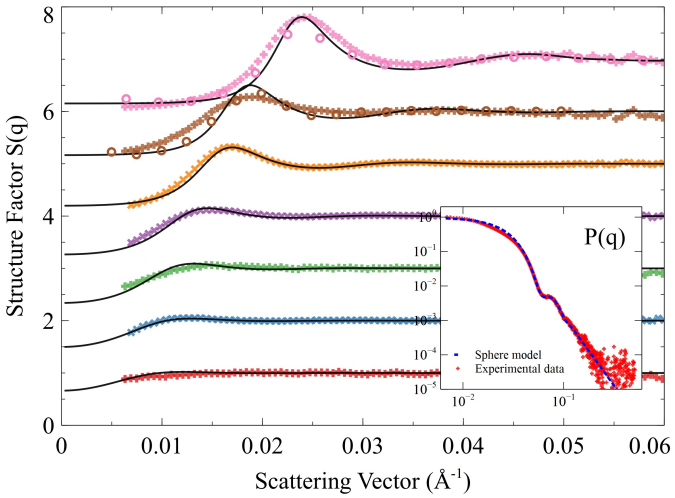

Fig. 4 Scattering data for Ludox HS40 silica nanoparticles. Main figure: structure factors shifted by steps of one for volume fractions $\phi =$ 0.00234, 0.0050, 0.00826, 0.0144, 0.0287, 0.0420 and 0.0907, from bottom to top. × and + symbols: experiments in two different chips. ○ symbls: simulations (see main text). Continuous lines: theory (see main text). Inset: intensity in dilute conditions (arbitrary units) and polydisperse sphere model for the form factor based on a Schulz distribution of radii with average 8 nm and 13 % polydispersity.

The slightly excessively marked peak in the theory for the sample at $\phi = 0.042$ is thus not due to the approximate treatment of polydispersity or a possible poor definition of the effective potential. As the experimental data seems close to that of a system with a smaller surface charge, a possible explanation could be an excessive acidification of the sample due to a prolonged exposition to ambient air.

Most importantly, the set of measurements on silica colloids and the comparison with theoretical and numerical models show that the meso-structure of interacting colloids can be measured quantitatively *in situ* and *operando* in a microfluidic chip, with a laboratory beamline. The photon flux is not really an issue here as silica is quite dense. The critical point for this kind of studies is the access to low wavenumbers since the value $S(q \to 0)$ is actually a direct measure of osmotic compressibility at least for monodisperse systems. Here we see that with the present setup where $q_{\min} \simeq 0.005\,\text{Å}^{-1}$, it can be measured for volume fractions above 5%. Note that increasing the sample-to-detector distance would not be an option here because the divergence of the beam actually sets the lowest observable angle. Improvements of the beam size and divergence would be very interesting to reach lower q values presently accessible only on synchrotrons.

Macromolecule in solution

The BSA model protein was used to evaluate the possibility to obtain good scattering data from macromolecules with the present chip and beamline setup. The corresponding scattering curves are presented in Figure 5. No interactions are supposed to appear for the most dilute sample. The intensity recorded for this sample is compared to two models in the inset of Figure 5. The first one is the form factor obtained from the known atomic structure of crystallized BSA from the Protein Data Bank (3v03.pdb). This form

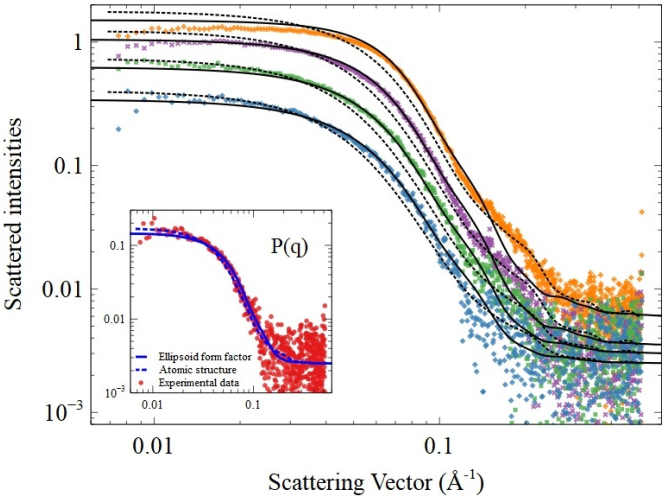

Fig. 5 Scattering data for different BSA concentrations: 100, 50, 25 and 12.5 mg/mL top to bottom (symbols), theory using the classical ellipsoid form factor (continuous lines) and using the form factor fitted from the BSA atomic structure (dashed lines). The inset shows data and theory for the most dilute sample: 5mg/mL.

factor was determined using CRYSOL from the ATSAS[67] package. The second model is the ellipsoid model classically used to coarse-grain the BSA structure, for a 4.74 nm equatorial radius and a 1.75 nm polar radius as in Ref. 68. Both models seem to be able to reproduce the dilute data within experimental uncertainty. The scattered intensity increases with concentration as expected. Even for the most concentrated case, the structure factor presents only a weak, hardly visible peak around $0.08\,\text{Å}^{-1}$ due to strong screening by the 0.15 mM PBS buffer. Interactions need to be accounted for, however, as the value $S(q\to 0)$ can be as low as about 0.5 for a BSA concentration of 100 g/L. Here, we found that using a unique value of $Z = 16$ unit charges per BSA molecule, with an effective radius $a = 3.4$ nm allowed to match the experimental data reasonably well. This is consistent with values found previously by similar fitting procedures,[68,69] and by *ab initio* calculations.[70] Note that the equation of state of BSA (osmotic pressure versus concentration) could also be predicted satisfactorily with these values.[70,71] The bump visible around $q = 0.2\,\text{Å}^{-1}$ especially for the most concentrated case is not an artifact. It cannot be reproduced with the ellipsoid model, but it is actually present in the structure factor extracted from the structure of crystallized BSA. Note that, however, using the latter form factor, the intensity at low q is significantly overestimated by the model. Determining the best coarse-graining strategy to model BSA is not the point of this work though, so we leave this issue open for future research. Here we have provided, using BSA, a proof of concept highlighting the potential of the present mirofluidic/SAXS setup to study the structure and interactions of macromolecules in solution.

Latex nanoparticles

The three types of colloids mentioned above and used for benchmarking the setup all have a significant contrast with their solvent, thus allowing rather straightforward measurements. The last type of sample considered is an aqueous dispersion of negatively charged sulfate latex beads in a 1mM NaCl buffer. These colloids were chosen as they are well characterized, but also have a low electronic contrast with water so their SAXS signature is among the most difficult to obtain quantitatively. Data were acquired for volume fractions ϕ =0.035, 0.07, 0.105, and 0.14. The acquisition time was set to one hour for each sample. As expected, the scattering curves presented in Figure 6 contain a significant amount of noise compared to the samples investigated above. The first structure peak is well resolved for the three most concentrated samples and its location follows the expected $\phi^{1/3}$ scaling due to long-range repulsions. The signal of the most dilute sample is quite difficult to fit with a form factor model because it is quite close to the background, and because of artifacts visible for $q < 0.01$ Å^{-1}. The latter are present because the slits were opened further to maximize the photon flux for this experiment. The same measurements were also performed in 1.5 mm diameter quartz capillaries in order to increase the signal to noise ratio, and the form factor corresponding to a polydisperse sphere model with radius 15 nm and polydispersity 16% was shown to fit the data quite well. This is consistent with the 13.5 nm average radius given by the manufacturer. In Figure 6, this form factor was used and structure has been calculated for an effective surface charge density σ=0.02 e/nm^2. This value is about one tenth of the bare surface charge density measured by titration, which is reasonable.

The use of latex nanospheres reveals the limits of laboratory SAXS measurements in microfluidic chips. The meso-structure of dispersions of small objects with low contrast such as polystyrene latex beads can be measured to some extent with acquisition times of the order of one hour but the poor signal-to-noise ratio makes attempts at modeling the data quite difficult. In order to improve this with the current setup, the pinhole could be positioned directly on the microfluidic chip, which would allow to open the slits further. However, since the pinhole is only at 2 cm from the sample now, this should not lead to a dramatic improvement of measurements. Another possible improvement of the setup would be to replace the solid anode source by a liquid-metal-jet or a rotating anode source, while keeping the use of the scatterless pinhole. This would probably allow an increase of at least one order of magnitude on the photon flux for the same small beam size compatible with on-chip measurements.

Conclusion

In summary, we established a proof-of-concept for a versatile microfluidic system coupled to a laboratory beamline for X-ray scattering experiments. The microfluidic chip was made of OSTEMER and polyimide, with very thin walls, to maximize the signal-to-noise ratio by minimizing absorption and background scattering by the device itself. This system shows great potential to study various dispersions and was successfully used to obtain structural information on both inorganic nanoparticles and bio-macromolecules in suspension. The form factor and the first structure peak of concentrated dispersions of repulsive colloids could be measured accurately. The second peak was more difficult to distinguish from the background noise. The zero wavenumber limit of the structure factor could be observed in dense systems

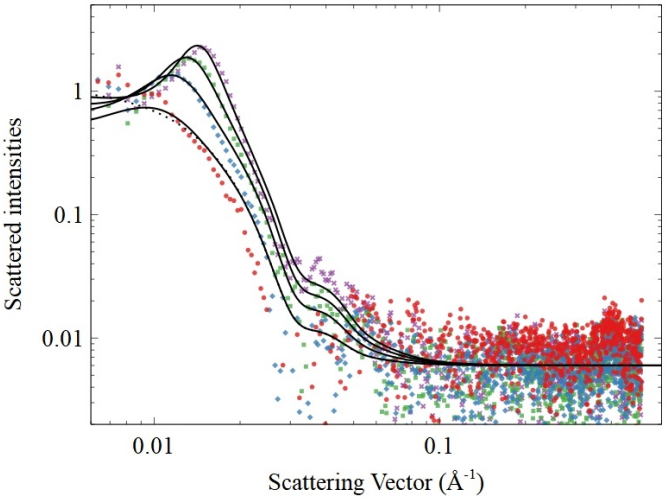

Fig. 6 Scattering data for latex nanoparticles (symbols) and Hard-Sphere-Yukawa theory (continuous lines). From top to bottom: initial dispersion ϕ= 0.14 and dilution factors 3/4, 1/2, and 1/4. The overall quality of the data is lower for low-contrast material

with the addition of a pinhole close to the sample. It allowed to open the slits of the beamline more than without pinhole, so the photon flux could be kept high enough despite the reduced beam size. A limitation of the device appeared for low-contrast materials such as polystyrene spheres suspended in water. The low quality of the data made quantitative fitting procedures difficult, although qualitative structural information could still be obtained. There is no doubt that using carefully chosen materials for microfluidic chips and state-of-the art laboratory beamlines with limited modifications now allows some *in situ*, *operando* SAXS measurements in the laboratory on a wide range of colloidal dispersions. The limited photon flux delivered by laboratory X-ray sources imposes significant acquisition times, ranging from seconds to tens of minutes. To perform time-resolved measurements in rapidly evolving systems, keeping a steady-state flow allows to associate a point in space to a time so long acquisitions can still be performed to observe fast transformations, although this may require large volumes of solutions. Time-resolved measurements on static samples can be undertaken for slowly evolving systems, as for example slow reactions, colloidal aggregation, rearrangements of the structure of metallic nanoparticles after synthesis, or processes involving slow solvent transfers such as osmotic compression[20] or solvent exchange. The simple setup investigated here opens the way to more sophisticated lab-on-chip devices in which *in-situ* scattering can be performed without the absolute need for a synchrotron facility.

Author Contributions

D. R. is the primary contributor who designed and built the microfluidic chips, performed the beamline experiments, prepared the bulk of the manuscript, and contributed to the data modelling. P. R. developed the SAXS equipment and performed the SAXS acquisition. M. M. and Y. H. contributed to SAXS data acquisition. Y. H. performed most of the modelling. M M., P. B., and Y. H. supervised this work. All parties contributed to the review and editing of the manuscript.

Conflicts of interest

There are no conflicts to declare.

Acknowledgements

We thank J.-B. Salmon, I. Rodriguez-Ruiz, and S. Teychené for discussions concerning microfluidic chips development, G. Nägele and M. Heinen for discussions concerning the modelling of the structure of polydisperse systems and for lending their OZ code to us, and Sébastien Lledos, Simon Tricard, Lise-Marie Lacroix and Guillaume Viau for providing the gold nanoparticles. We acknowledge the ANR program Grant No. ANR-18-CE06-0021 for financial support. This work was performed using HPC resources from CALMIP (Grant 2023A-P21039).

Notes and references

1 L. Feigin, D. I. Svergun *et al.*, *Structure analysis by small-angle X-ray and neutron scattering*, Springer, 1987, vol. 1.
2 O. Glatter, O. Kratky and H. Kratky, *Small angle X-ray scattering*, Academic press, 1982.
3 A. Guinier, G. Fournet and K. L. Yudowitch, *Small-angle scattering of X-rays*, Wiley New York, 1955.
4 A. Ducruix, J. P. Guilloteau, M. Riès-Kautt and A. Tardieu, *Journal of Crystal Growth*, 1996, **168**, 28–39.
5 H. Fischer, M. d. Oliveira Neto, H. B. Napolitano, I. Polikarpov and A. F. Craievich, *Journal of Applied Crystallography*, 2010, **43**, 101–109.
6 H. D. T. Mertens and D. I. Svergun, *Journal of Structural Biology*, 2010, **172**, 128–141.
7 H. Durchschlag, P. Zipper, G. Purr and R. Jaenicke, *Colloid and Polymer Science*, 1996, **274**, 117–137.
8 P. R. A. F. Garcia, O. Prymak, V. Grasmik, K. Pappert, W. Wlysses, L. Otubo, M. Epple and C. L. P. Oliveira, *Nanoscale Advances*, 2020, **2**, 225–238.
9 W. Wang, X. Chen, Q. Cai, G. Mo, L. S. Jiang, K. Zhang, Z. J. Chen, Z. H. Wu and W. Pan, *The European Physical Journal B*, 2008, **65**, 57–64.
10 M. Harada, N. Tamura and M. Takenaka, *The Journal of Physical Chemistry C*, 2011, **115**, 14081–14092.
11 P. Garg, G. Kaur, G. R. Chaudhary, S. L. Gawali and P. A. Hassan, *Journal of Molecular Liquids*, 2018, **271**, 157–165.
12 T. Uzawa, T. Kimura, K. Ishimori, I. Morishima, T. Matsui, M. Ikeda-Saito, S. Takahashi, S. Akiyama and T. Fujisawa, *Journal of Molecular Biology*, 2006, **357**, 997–1008.
13 D. Mark, S. Haeberle, G. Roth, F. v. Stetten and R. Zengerle, *Chemical Society Reviews*, 2010, **39**, 1153–1182.
14 A. Aryasomayajula, P. Bayat, P. Rezai and P. R. Selvaganapathy, *Springer handbook of nanotechnology*, 2017, 487–536.
15 C.-Y. Lee, C.-L. Chang, Y.-N. Wang and L.-M. Fu, *International Journal of Molecular Sciences*, 2011, **12**, 3263–3287.
16 K. Ward and Z. H. Fan, *Journal of micromechanics and microengineering : structures, devices, and systems*, 2015, **25**, 094001.
17 M. Yamada and M. Seki, *Lab on a Chip*, 2005, **5**, 1233–1239.
18 A. S. Clark and A. San-Miguel, *Lab on a Chip*, 2021, **21**, 3762–3774.
19 X. Qiu, J. A. Lombardo, T. M. Westerhof, M. Pennell, A. Ng, H. Alshetaiwi, B. M. Luna, E. L. Nelson, K. Kessenbrock, E. E. Hui and J. B. Haun, *Lab on a Chip*, 2018, **18**, 2776–2786.
20 C. Keita, Y. Hallez and J.-B. Salmon, *Physical Review E*, 2021, **104**, L062601.
21 J. Leng and J.-B. Salmon, *Lab on a Chip*, 2009, **9**, 24–34.
22 H.-h. Shi, Y. Xiao, S. Ferguson, X. Huang, N. Wang and H.-x. Hao, *Lab on a Chip*, 2017, **17**, 2167–2185.
23 S. Teychené and B. Biscans, *Crystal Growth & Design*, 2011, **11**, 4810–4818.
24 X. Chen, D. F. Cui, C. C. Liu and H. Li, *Sensors and Actuators B: Chemical*, 2008, **130**, 216–221.
25 S. Choi, S. Song, C. Choi and J.-K. Park, *Lab on a Chip*, 2007, **7**, 1532–1538.
26 T. A. Thorsen, *BioTechniques*, 2004, **36**, 197–199.
27 P. De Stefano, E. Bianchi and G. Dubini, *Biomicrofluidics*, 2022, **16**, 031501.
28 E. M. Payne, D. A. Holland-Moritz, S. Sun and R. T. Kennedy, *Lab on a Chip*, 2020, **20**, 2247–2262.
29 D. Radajewski, L. Hunter, X. He, O. Nahi, J. M. Galloway and F. C. Meldrum, *Lab on a Chip*, 2021, **21**, 4498–4506.
30 X. Chen, J. Wang, R. Pan, S. Roth and S. Förster, *The Journal of Physical Chemistry C*, 2021, **125**, 1087–1095.
31 T. Lange, S. Charton, T. Bizien, F. Testard and F. Malloggi, *Lab on a Chip*, 2020, **20**, 2990–3000.

32 R. Stehle, G. Goerigk, D. Wallacher, M. Ballauff and S. Seiffert, *Lab on a Chip*, 2013, **13**, 1529–1537.
33 A. M. Karim, N. Al Hasan, S. Ivanov, S. Siefert, R. T. Kelly, N. G. Hallfors, A. Benavidez, L. Kovarik, A. Jenkins, R. E. Winans and A. K. Datye, *The Journal of Physical Chemistry C*, 2015, **119**, 13257–13267.
34 N. Iranpour Anaraki, M. Liebi, K. Iranshahi, C. Blanchet, P. Wick and A. Neels, *ACS Applied Nano Materials*, 2022, **5**, 18921–18929.
35 K. N. Toft, B. Vestergaard, S. S. Nielsen, D. Snakenborg, M. G. Jeppesen, J. K. Jacobsen, L. Arleth and J. P. Kutter, *Analytical chemistry*, 2008, **80**, 3648–3654.
36 M. Arai, E. Kondrashkina, C. Kayatekin, C. R. Matthews, M. Iwakura and O. Bilsel, *Journal of Molecular Biology*, 2007, **368**, 219–229.
37 J. Lipfert, V. B. Chu, Y. Bai, D. Herschlag and S. Doniach, *Journal of Applied Crystallography*, 2007, **40**, s229–s234.
38 L. Pollack, M. W. Tate, A. C. Finnefrock, C. Kalidas, S. Trotter, N. C. Darnton, L. Lurio, R. H. Austin, C. A. Batt, S. M. Gruner and S. G. J. Mochrie, *Physical review letters*, 2001, **86**, 4962–4965.
39 S. Köster, J. B. Leach, B. Struth, T. Pfohl and J. Y. Wong, *Langmuir: the ACS journal of surfaces and colloids*, 2007, **23**, 357–359.
40 M. Elisabeth Brennich, J.-F. Nolting, C. Dammann, B. Nöding, S. Bauch, H. Herrmann, T. Pfohl and S. Köster, *Lab on a Chip*, 2011, **11**, 708–716.
41 E. Ilhan-Ayisigi, B. Yaldiz, G. Bor, A. Yaghmur and O. Yesil-Celiktas, *Colloids and Surfaces B: Biointerfaces*, 2021, **201**, 111633.
42 N. Pham, D. Radajewski, A. Round, M. Brennich, P. Pernot, B. Biscans, F. Bonneté and S. Teychené, *Analytical Chemistry*, 2017, **89**, 2282–2287.
43 J. P. Lafleur, D. Snakenborg, S. S. Nielsen, M. Møller, K. N. Toft, A. Menzel, J. K. Jacobsen, B. Vestergaard, L. Arleth and J. P. Kutter, *Journal of Applied Crystallography*, 2011, **44**, 1090–1099.
44 J. B. Hopkins and R. E. Thorne, *Journal of Applied Crystallography*, 2016, **49**, 880–890.
45 T. Skarzynski, *Acta Crystallographica Section D-Biological Crystallography*, 2013, **69**, 1283–1288.
46 O. Tache, S. Rouziere, P. Joly, M. Amara, B. Fleury, A. Thill, P. Launois, O. Spalla and B. Abecassis, *Journal of Applied Crystallography*, 2016, **49**, 1624–1631.
47 M. Herbst, E. Hofmann and S. Förster, *Langmuir*, 2019, **35**, 11702–11709.
48 J. Polte, R. Erler, A. F. Thünemann, S. Sokolov, T. T. Ahner, K. Rademann, F. Emmerling and R. Kraehnert, *ACS nano*, 2010, **4**, 1076–1082.
49 X. Chen, J. Schröder, S. Hauschild, S. Rosenfeldt, M. Dulle and S. Förster, *Langmuir: the ACS journal of surfaces and colloids*, 2015, **31**, 11678–11691.
50 M. A. Levenstein, K. Robertson, T. D. Turner, L. Hunter, C. O'Brien, C. O'Shaughnessy, A. N. Kulak, P. Le Magueres, J. Wojciechowski, O. O. Mykhaylyk, N. Kapur and F. C. Meldrum, *IUCrJ*, 2022, **9**, 538–543.
51 C. E. Hoyle and C. N. Bowman, *Angewandte Chemie International Edition*, 2010, **49**, 1540–1573.
52 T. Kister, D. Monego, P. Mulvaney, A. Widmer-Cooper and T. Kraus, *ACS nano*, 2018, **12**, 5969–5977.
53 M. Kotlarchyk and S.-H. Chen, *The Journal of chemical physics*, 1983, **79**, 2461–2469.
54 T. Zemb and P. Lindner, *Neutron, X-rays and light. Scattering methods applied to soft condensed matter*, North Holland, 2002.
55 J. Chang, P. Lesieur, M. Delsanti, L. Belloni, C. Bonnet-Gonnet and B. Cabane, *The Journal of Physical Chemistry*, 1995, **99**, 15993–16001.
56 J. Li, B. Cabane, M. Sztucki, J. Gummel and L. Goehring, *Langmuir*, 2012, **28**, 200–208.
57 B. Cabane, J. Li, F. Artzner, R. Botet, C. Labbez, G. Bareigts, M. Sztucki and L. Goehring, *Physical Review Letters*, 2016, **116**, 208001.
58 V. Goertz, N. Dingenouts and H. Nirschl, *Particle & Particle Systems Characterization*, 2009, **26**, 17–24.
59 Y. Hallez and M. Meireles, *Langmuir*, 2017, **33**, 10051–10060.
60 G. Nägele, *Physics Reports*, 1996, **272**, 215–372.
61 N. Boon, G. I. Guerrero-García, R. Van Roij and M. Olvera de la Cruz, *Proceedings of the National Academy of Sciences*, 2015, **112**, 9242–9246.
62 G. Trefalt, S. H. Behrens and M. Borkovec, *Langmuir*, 2016, **32**, 380–400.
63 M. Fushiki, *The Journal of chemical physics*, 1992, **97**, 6700–6713.
64 J. Dobnikar, D. Haložan, M. Brumen, H.-H. Von Grünberg and R. Rzehak, *Computer physics communications*, 2004, **159**, 73–92.
65 Y. Hallez, J. Diatta and M. Meireles, *Langmuir*, 2014, **30**, 6721–6729.
66 Y. Hallez and M. Meireles, *Langmuir*, 2016, **32**, 10430–10444.
67 D. Franke, M. V. Petoukhov, P. V. Konarev, A. Panjkovich, A. Tuukkanen, H. D. T. Mertens, A. G. Kikhney, N. R. Hajizadeh, J. M. Franklin, C. M. Jeffries and D. I. Svergun, *Journal of Applied Crystallography*, 2017, **50**, 1212–1225.
68 M. Heinen, F. Zanini, F. Roosen-Runge, D. Fedunová, F. Zhang, M. Hennig, T. Seydel, R. Schweins, M. Sztucki, M. Antalík *et al.*, *Soft Matter*, 2012, **8**, 1404–1419.
69 F. Zhang, M. W. A. Skoda, R. M. J. Jacobs, R. A. Martin, C. M. Martin and F. Schreiber, *The Journal of Physical Chemistry B*, 2007, **111**, 251–259.
70 F. Petrosino, Y. Hallez, G. De Luca and S. Curcio, *Chemical Engineering Science*, 2020, **224**, 115762.
71 W. R. Bowen and P. M. Williams, *Journal of colloid and interface science*, 1996, **184**, 241–250.